




Structural, optical and magnetic properties of Sr and Ni co-doped YFeO₃ nanoparticles prepared by simple co-precipitation method

Duyen H. T. Pham¹, Linh T. Tr. Nguyen², V. O. Mittova³, Diem H. Chau², I. Ya. Mittova⁴, Tien A. Nguyen², and Vuong X. Bui^{5,*} 

¹Thu Dau Mot University, Thu Dau Mot City, Binh Duong Province 590000, Vietnam

²Ho Chi Minh City University of Education, Ho Chi Minh City 700000, Vietnam

³Voronezh State Medical University Named after N. N. Burdenko, Voronezh 394036, Russia

⁴Voronezh State University, Voronezh 394018, Russia

⁵Sai Gon University, Ho Chi Minh City 700000, Vietnam

Received: 5 January 2022

Accepted: 30 April 2022

Published online:

26 May 2022

© The Author(s), under exclusive licence to Springer Science+Business Media, LLC, part of Springer Nature 2022, corrected publication 2022

ABSTRACT

YFeO_{3+δ}, Y_{0.8}Sr_{0.2}FeO_{3+δ}, YFe_{0.8}Ni_{0.2}O_{3+δ}, and Y_{0.8}Sr_{0.2}Fe_{0.8}Ni_{0.2}O_{3+δ} nanoparticles have been successfully synthesized by a simple co-precipitation technique. Results obtained using thermogravimetry and differential scanning calorimetry, powder X-ray diffraction, transmission electron microscopy indicate that YFeO₃, Sr-doped YFeO₃, Ni-doped YFeO₃, and Sr and Ni co-doped YFeO₃ nanoparticles with orthorhombic structure were fabricated at 800 °C for 1 h. The obtained materials have the crystallite sizes below 30 nm and particle sizes below 40 nm. Sr and/or Ni doping led to the distortion of the YFeO₃ crystal structure and thus altered the magnetic properties of the corresponding materials. The Sr-doped YFeO₃, Sr and Ni co-doped YFeO₃, and especially Ni-doped YFeO₃ samples have significantly higher absorbance in the visible light region (~ 400–800 nm) and lower band gap than those of pure YFeO₃ sample. Magnetic hysteresis loop analyses illustrate that ferromagnetic behavior of the YFeO₃ nanopowders can be strongly enhanced with the addition of Sr and/or Ni. The coercivity and remanent magnetization of Sr and Ni co-doped YFeO_{3+δ} are, respectively, around 80 and 104 times higher than those of the pure YFeO_{3+δ} sample. The excellent optical and magnetic properties of Sr and Ni co-doped YFeO_{3+δ} nanomaterials suggest great potential for applications related to optics and magnetism.

Address correspondence to E-mail: buixuanvuongsgu@gmail.com

1 Introduction

Yttrium iron oxide (YFeO₃) is a LnFeO₃ perovskite orthoferrite having an orthorhombic structure [1–3]. Orthoferrite yttrium (*o*-YFeO₃) has been attracting much interest in both fundamental research and applied science [4, 5]. The structure and properties of *o*-YFeO₃ materials depend on many factors such as particle shape and size, crystallite size, preparation method and especially, on the nature and concentration of the dopants in *o*-YFeO₃ crystal lattice [6–8]. The partial doping at the site of Y³⁺ or Fe³⁺ in the lattice of YFeO₃ can lead to multiple oxidation states and crystal defects, and thus, to changes in the properties of the materials [9–12]. The perovskite-type structure can be discriminated by the Goldschmidt tolerance factor (*t*), which can be calculated following the Eq. (1) [13–17].

$$t = \frac{r_A + r_O}{\sqrt{2}(r_B + r_O)}, \quad (1)$$

where r_A, r_B and r_O are the radii of large cation A, small cation B and anion O²⁻, respectively. For $t = 1$, perovskite ABO₃ has an ideal cubic structure. In cases where $0.75 < t < 0.9$, the structure of ABO₃ is orthorhombic. For *o*-YFeO₃ with the radii of Y³⁺ = 0.094, Fe³⁺ = 0.065, and O²⁻ = 0.126 nm, we have $t = 0.82$ [8]. In all cases of $t \neq 1$, the crystal lattice is distorted, the B–O–B bond angle is no longer 180° but bent, and the B–O bond lengths are different in different directions. The ABO₃ structure is modified, resulting in the alteration of its electrical, magnetic, and optical properties [18–21].

Besides, according to Goldschmidt's rules, in order to form a homogenous solid solution at a temperature largely different from the melting points of the components, the difference between the ionic radii of the cation and its dopant (Δr) should not exceed 15%, i.e., $\Delta r/r \leq 15\%$ (r is the radius of the smaller cation) [10]. Indeed, according to [10], Ba-doped YFeO₃ nanomaterials were successfully synthesized by the sol-gel method, followed by calcination of the precursor at 750 °C for 1 h. The results showed that the substitution of Ba²⁺ in the crystal lattice of YFeO₃ only happened with $x = 0.1$. For $x > 0.1$, besides the orthorhombic phase YFeO₃, XRD peaks of Y₂O₃, BaO, and BaY₂O₄ were also observed. The doping of Ba²⁺ in YFeO₃ increased the crystallite size from 30 ± 2 nm (for YFeO₃) to 55 ± 5 nm (for

Y_{0.9}Ba_{0.1}FeO₃). Barium-doped yttrium orthoferrite with $x = 0.1$ underwent qualitative transformation from a soft to a hard magnetic material, with H_c increased from 70 to 1000 Oe [22]. The structural defects, leading to changes in the magnetic properties of Ba-doped YFeO₃ nanomaterials, can be explained by the large difference between the radii of the cations Y³⁺ (0.094 nm) and Ba²⁺ (0.134 nm) ($\Delta r = 0.04$ nm). Even with a small Δr ($\Delta r \neq 0$), Mn-doped YFeO₃ orthoferrite also underwent significant changes in the structure and properties [11]. The YFe_{1-x}Mn_xO₃ series ($x = 0, 0.05, 0.1, 0.15,$ and 0.2) orthorhombic nanomaterials were prepared by the citric acid sol-gel method and annealing of the precursor at 800 °C for 2 h [11], showing the domination of YFeO₃ hexagonal structure when the calcination temperature (T°) < 800 °C or $x > 0.2$. When the Mn concentration in the YFeO₃ orthorhombic crystal lattice increased, particle size increased from 50 to 90 nm and saturation magnetization (M_s) increased from 0.015 to 0.08 emu g⁻¹ for YFeO₃ and YFe_{0.8}Mn_{0.2}O₃, respectively. The partial replacement of Y³⁺ or Fe³⁺ by another metal cation also affected the optical properties of the YFeO₃ material. Indeed, the doping of Sm³⁺ in YFeO₃ orthorhombic structure decreased H_c and absorbance in the visible range (~ 400–600 nm), while increased M_s (emu g⁻¹) and E_g (eV) [12]. In this work, Y_{1-x}Sm_xFeO₃ ($x = 0, 0.05, 0.1,$ and 0.15) orthorhombic materials of 300–1200 μm were synthesized by the citric acid sol-gel method and annealing of the precursor at 900 °C for 8 h.

In our previous publication [23], YFe_{1-x}Ni_xO₃ nanomaterials were prepared by a simple co-precipitation method with KOH 5% solution as the precipitating agent. Single phase orthorhombics YFe_{1-x}Ni_xO₃ ($x = 0, 0.1, 0.15, 0.2,$ and 0.25) were formed after annealing the precipitates at 800 °C for 1 h. NiO and Y₂O₃ appeared as impurities when $T^\circ > 800$ °C or $x > 0.25$. The substitution of Ni with an yttrium iron oxide lattice also increased the crystallite size and magnetic characteristics of the materials. However, to the best of our knowledge, the simultaneous doping of two different metal cations (specifically Sr²⁺ and Ni²⁺) to both Y³⁺ and Fe³⁺ positions in YFeO₃ crystal lattice has not yet been reported.

Thus, the aim of this work is to study of how the doping of strontium and nickel, individually and simultaneously, affected the structure, the optical and magnetic properties of YFeO₃ orthorhombic nanomaterials. Based on previous works [10–12, 23, 24],

the concentration of dopants was 20% molar ratio, corresponding to the empirical formulae of $YFeO_3$, $Y_{0.8}Sr_{0.2}FeO_3$, $YFe_{0.8}Ni_{0.2}O_3$, and $Y_{0.8}Sr_{0.2}Fe_{0.8}Ni_{0.2}O_3$.

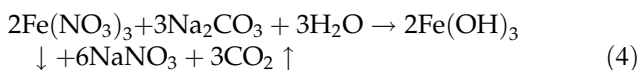
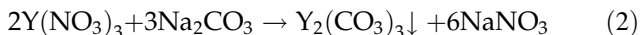
2 Experimental

2.1 Materials and methods

$Y(NO_3)_3 \cdot 6H_2O$ (99.9% purity, Sigma-Aldrich), $Ni(NO_3)_2 \cdot 6H_2O$ (99.8% purity, Acros Organic), $Fe(NO_3)_3 \cdot 9H_2O$ (99.6% purity, Sigma-Aldrich), $Sr(NO_3)_2$ (99.9% purity, Sigma-Aldrich), $Na_2CO_3 \cdot 10H_2O$ (99.7% purity, Merck), and double distilled water were employed as the starting materials.

$Y_{1-x}Sr_xFe_{1-y}Ni_yO_3$ nanoparticles were synthesized by a simple co-precipitation method based on the preparation of $YFe_{1-x}Ni_xO_3$ [23]. Instead of KOH 5%, Na_2CO_3 was used as the precipitating agent because Sr^{2+} cations cannot be precipitated by OH^- anions [25].

50 mL of the aqueous solution containing the mixture of $Y(NO_3)_3$, $Sr(NO_3)_2$, $Fe(NO_3)_3$ and $Ni(NO_3)_2$ with the molar ratio of $Y^{3+}:Sr^{2+}:Fe^{3+}:Ni^{2+} = (1-x):x:(1-y):y$ (for 4 series of materials: (1) $YFeO_3$ ($x = y = 0$), (2) $Y_{0.8}Sr_{0.2}FeO_3$ ($x = 0.2, y = 0$), (3) $YFe_{0.8}Ni_{0.2}O_3$ ($x = 0, y = 0.2$), and (4) $Y_{0.8}Sr_{0.2}Fe_{0.8}Ni_{0.2}O_3$ ($x = y = 0.2$)) was added dropwise to 400 mL of boiling double distilled water on a heating stirrer ($T^\circ > 95^\circ C$). The mixture was then boiled for another 10 min before being cooled down to room temperature ($\sim 30^\circ C$). Next, 50 mL of Na_2CO_3 5% solution was added dropwise to the system while continuously stirring. The amount of Na_2CO_3 5% solution was enough to precipitate all the cations according to the chemical Eqs. (2, 3, 4, 5) [25, 26].



After the addition of the Na_2CO_3 5% solution, the system was stirred for 1 h to homogeneously disperse the precipitates. The precipitates were subsided for 30 min then filtered and washed by double distilled water until pH 7 (the filtrate was checked by pH paper). The obtained solid was left to dry at room temperature for 3–5 days then ground, resulting in

brownish yellow powder (precursor for $Y_{1-x}Sr_xFe_{1-y}Ni_yO_3$ nanoparticles).

2.2 Characterization

Thermogravimetry and differential scanning calorimetry (TG–DSC) curves of the precursor for the synthesis of $YFeO_3$ nanoparticles were recorded under dry air at the heating rate of $10 K \cdot min^{-1}$, maximum temperature of $1000^\circ C$, platinum crucibles, using a Labsys Evo (France).

Powder X-ray diffraction analysis (PXRD) of the obtained $Y_{1-x}Sr_xFe_{1-y}Ni_yO_3$ samples was carried out using a D8-ADVANCE X-ray diffractometer (Germany) (CuK_α radiation, $\lambda = 1.5406 \text{ \AA}$, angle range of $2\theta = 10^\circ - 80^\circ$, scanning step of $0.19^\circ s^{-1}$). The crystallite sizes of $Y_{1-x}Sr_xFe_{1-y}Ni_yO_3$ (D_{XRD} , nm) were determined based on Scherrer's equation [4, 27].

$$D = \frac{0.89\lambda}{(FWHM) \cos \theta}, \quad (6)$$

where FWHM is the full-width at half maximum, and θ is the diffraction angle of the maximum reflection.

Lattice constants ($a; b; c, \text{ \AA}$) and unit cell volume ($V, \text{ \AA}^3$) were calculated using the formulas presented in Ref [27]:

$$\frac{1}{d^2} = \frac{h^2}{a^2} + \frac{k^2}{b^2} + \frac{l^2}{c^2}, \quad (7)$$

$$V = a \cdot b \cdot c. \quad (8)$$

The morphology and particle size were investigated by transmission electron microscopy (TEM; Jeol-1400, Japan).

The quantitative and qualitative composition of the samples was determined by energy dispersive X-ray spectroscopy (EDX-analysis) using an FE-SEM S-4800 scanning electron microscope (Japan). The quantitative elemental composition was determined as the average of the values obtained at five different points of each sample.

The UV–Vis absorption spectra of the $Y_{1-x}Sr_xFe_{1-y}Ni_yO_3$ nanopowders were studied on a UV–visible spectrophotometer (UV–Vis; JASCO V–550, Japan). The optical energy gap (E_g , eV) was determined by fitting the absorption data to the direct transition as Eq. (9):

$$Ah\nu = \sqrt{\alpha(h\nu - E_g)}, \quad (9)$$

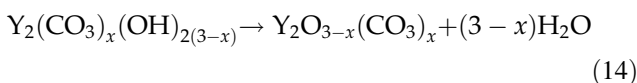
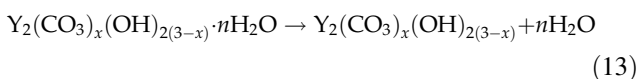
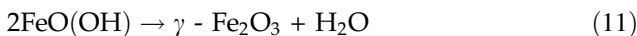
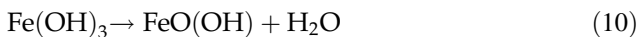
where A is the optical absorption coefficient, $h\nu$ is the photon energy, E_g is the direct band gap and α is a constant [28]. The extrapolation of the linear portions of the curves toward absorption equal to zero ($y = 0$) gives E_g for direct transitions.

The hysteresis loop and magnetic properties including coercive force (H_c , Oe), remanent magnetization (M_r , emu g^{-1}) and saturation magnetization (M_s , emu g^{-1}) were recorded at 300 K on a vibrating sample magnetometer (VSM, MICROSENE EV11, Japan) under a magnetic field in the range of $-16\,000$ Oe to $+16\,000$ Oe.

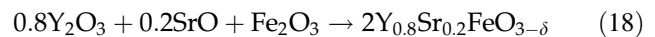
3 Result and discussion

As the radii of Fe^{3+} (0.065 nm) and Ni^{3+} (0.061 nm) are approximate while those of Y^{3+} (0.094 nm) and Sr^{2+} (0.112 nm) have a big difference ($\Delta r = 0.018$ nm) [25], the two precursors for $YFeO_3$ and $Y_{0.8}Sr_{0.2}FeO_3$ nanoparticles were chosen for TG–DSC analysis. The results are shown in Fig. 1.

The TG curves of two samples ($YFeO_3$ and $Y_{0.8}Sr_{0.2}FeO_3$) from room temperature to $1000\text{ }^\circ C$ are quite similar. The mass loss percentage are 32.81% for $YFeO_3$ and 31.25% for $Y_{0.8}Sr_{0.2}FeO_3$, and become negligible at around $750\text{ }^\circ C$ for both samples (according to TG curves). Those results can be derived from their resemblance to the average atomic masses of yttrium and strontium, and the formation of stable carbonate precipitates of both Y^{3+} and Sr^{2+} cations ($Y = 88.91$, $Sr = 87.62$) [25]. The mass losses of the samples when heated were from the dehydration of moisture, dehydration by pyrolysis of iron precipitates, and carbon dioxide loss by base–carbonate pyrolysis of yttrium and strontium carbonate according to the chemical Eqs. (10, 11, 12, 13, 14, 15, 16) [30–33].



The thermal behaviors of $YFeO_3$ and $Y_{0.8}Sr_{0.2}FeO_3$ samples also have similarity in their endothermic peaks at $128.86\text{ }^\circ C/133.33\text{ }^\circ C$ and exothermic peaks at $302.13\text{ }^\circ C/321.90\text{ }^\circ C$ on the DSC curves, respectively. The endothermic effects at $70\text{--}200\text{ }^\circ C$ come from the removal of moisture, dehydration by pyrolysis of iron (III) and of yttrium and strontium precipitates [25, 30, 31, 33]. The exothermic peaks at $200\text{--}400\text{ }^\circ C$ correspond to the $\gamma\text{-}Fe_2O_3 \rightarrow \alpha\text{-}Fe_2O_3$ phase transition according to Eq. (12) [30, 32]. The only difference in the thermal behaviors of $YFeO_3$ and $Y_{0.8}Sr_{0.2}FeO_3$ is the absence of the endothermic peak at $450.17\text{ }^\circ C$ for the $YFeO_3$ sample. This difference originates from the carbonate hydrolysis according to Eq. (16), resulting in a stronger endothermic effect. Finally, exothermic peaks at $700\text{--}800\text{ }^\circ C$ were observable for both samples, which indicates the perovskite phase formation as shown in Eqs. (17) and (18).

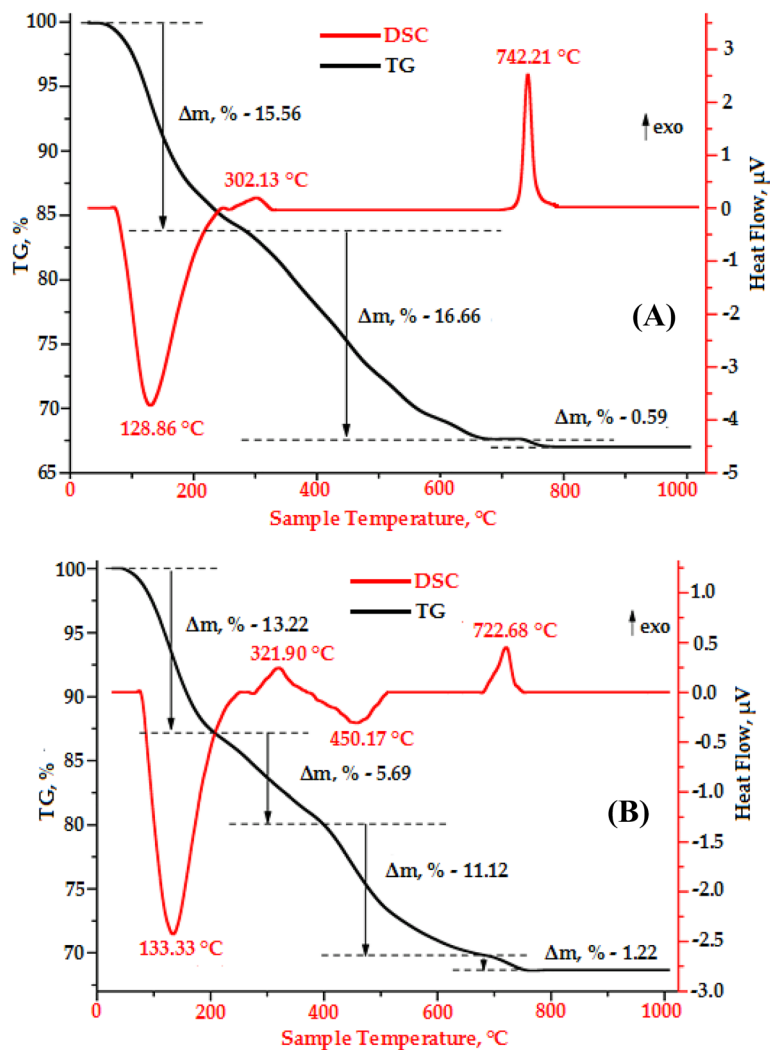


From the above TG–DSC analysis and previous synthesis of $YFe_{1-x}Mn_xO_3$ [11], $Y_{1-x}Sm_xFeO_3$ [12], and $YFe_{1-x}Ni_xO_3$ [23] nanoparticles, the precipitates $YFeO_3$ and $Y_{1-x}Sr_xFe_{1-y}Ni_yO_3$ were annealed at $800\text{ }^\circ C$ for 1 h, followed by a structural analysis with PXRD.

The PXRD pattern of the $YFeO_3$ sample (Fig. 2A) has the specific peaks of the $YFeO_3$ orthorhombic phase, $Pnma$ (62) space group (JCPDS: 00-039-1489). The good crystallinity of the $YFeO_3$ sample is proven by its high peak intensity and flat, fine baseline, and no minor impurity peaks were present.

The PXRD patterns of the doped and co-doped nanopowders indicate the same characteristic shape as that of the pristine $YFeO_3$ pattern, with a slight shift in the positions of the peaks (Fig. 2B and Table 1). This is a normal situation for the $YFeO_3$ perovskite, involving the difference in the radii of the cations, according to Goldschmidt [24]. Table 1 shows that, compared to pure $YFeO_3$, 2θ values underwent a left-shift by doping Sr^{2+} with a bigger radius than that of Y^{3+} , while the doping of Ni^{3+} with smaller radius than that of Fe^{3+} resulted in a right-shift of 2θ positions. For Sr and Ni co-doped $YFeO_3$ samples, 2θ positions also had a right-shift. Similar results were

Fig. 1 The TG–DSC curves of the precipitate sample corresponding to YFeO_3 nanoparticles (A) and $\text{Y}_{0.8}\text{Sr}_{0.2}\text{FeO}_3$ nanoparticles (B)



reported for Gd and Co co-doped YFeO_3 nanopowders [28]. Thus, it is evident that Sr^{2+} and Ni^{3+} replaced the Y^{3+} and Fe^{3+} ions in YFeO_3 , respectively. The shift of 2θ values is also consistent with the changes in the crystallite size (D_{XRD} , nm) and lattice cell volume (V , \AA^3) (Table 1).

Table 1 shows the structural characteristics of $\text{Y}_{1-x}\text{Sr}_x\text{Fe}_{1-y}\text{Ni}_y\text{O}_3$ nanocrystals. The crystallite size (D_{XRD} , nm) and unit cell volume (V , \AA^3) of $\text{YFeO}_{3\pm\delta}$ increased with an increase in Sr content and decreased with the addition of Ni because $r_{\text{Sr}^{2+}} > r_{\text{Y}^{3+}}$, while $r_{\text{Ni}^{3+}} < r_{\text{Fe}^{3+}}$. This is another indication of the successful substitution of Y^{3+} and Fe^{3+} ions in the YFeO_3 lattice by Sr^{2+} and Ni^{2+} ions. The smallest values of D_{XRD} and V correspond to Sr and Ni co-doped YFeO_3 samples, because the simultaneous substitution of Y^{3+} and Fe^{3+} by Sr^{2+} and Ni^{3+} led to an increase in the amount of oxidized Fe^{3+} to form

Fe^{4+} compared to $\text{Y}_{0.8}\text{Sr}_{0.2}\text{FeO}_{3\pm\delta}$ and $\text{YFe}_{0.8}\text{Ni}_{0.2}\text{O}_3$ ($r_{\text{Fe}^{4+}} < r_{\text{Fe}^{3+}}$), resulting in the decrease in D_{XRD} and V according to Vegard's law [14, 20, 34, 35]. This result is also in good agreement with the TEM images of $\text{Y}_{1-x}\text{Sr}_x\text{Fe}_{1-y}\text{Ni}_y\text{O}_3$ samples in Fig. 3.

The TEM images in Fig. 3 show that the obtained $\text{Y}_{1-x}\text{Sr}_x\text{Fe}_{1-y}\text{Ni}_y\text{O}_3$ samples are composed of spherical or slightly angular-shaped particles. The average particle sizes of the test samples of YFeO_3 , $\text{Y}_{0.8}\text{Sr}_{0.2}\text{O}_3$, $\text{YFe}_{0.8}\text{Ni}_{0.2}\text{O}_3$, and $\text{Y}_{0.8}\text{Sr}_{0.2}\text{Fe}_{0.8}\text{Ni}_{0.2}\text{O}_3$ were approximately 35.17, 39.86, 34.85, and 32.43 nm, respectively. However, aggregations and clusters are still observable, maybe due to the strong magnetic interaction between the particles.

Elemental composition analysis from EDX shows no impurity elements apart from Y, Sr, Fe, Ni, and O which were detected in the $\text{Y}_{1-x}\text{Sr}_x\text{Fe}_{1-y}\text{Ni}_y\text{O}_3$ nanomaterials (Fig. 4). The percentage of atoms of each

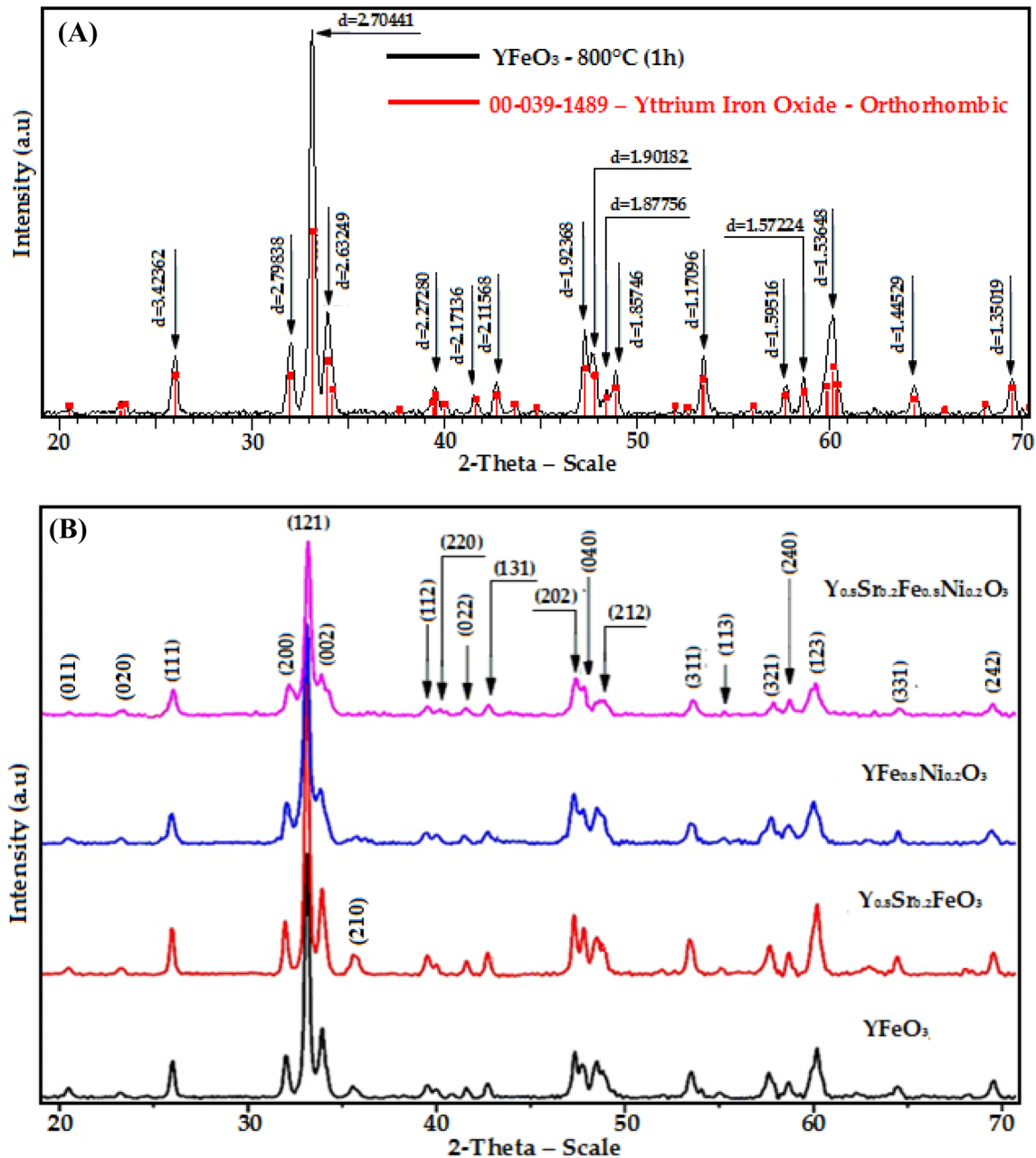


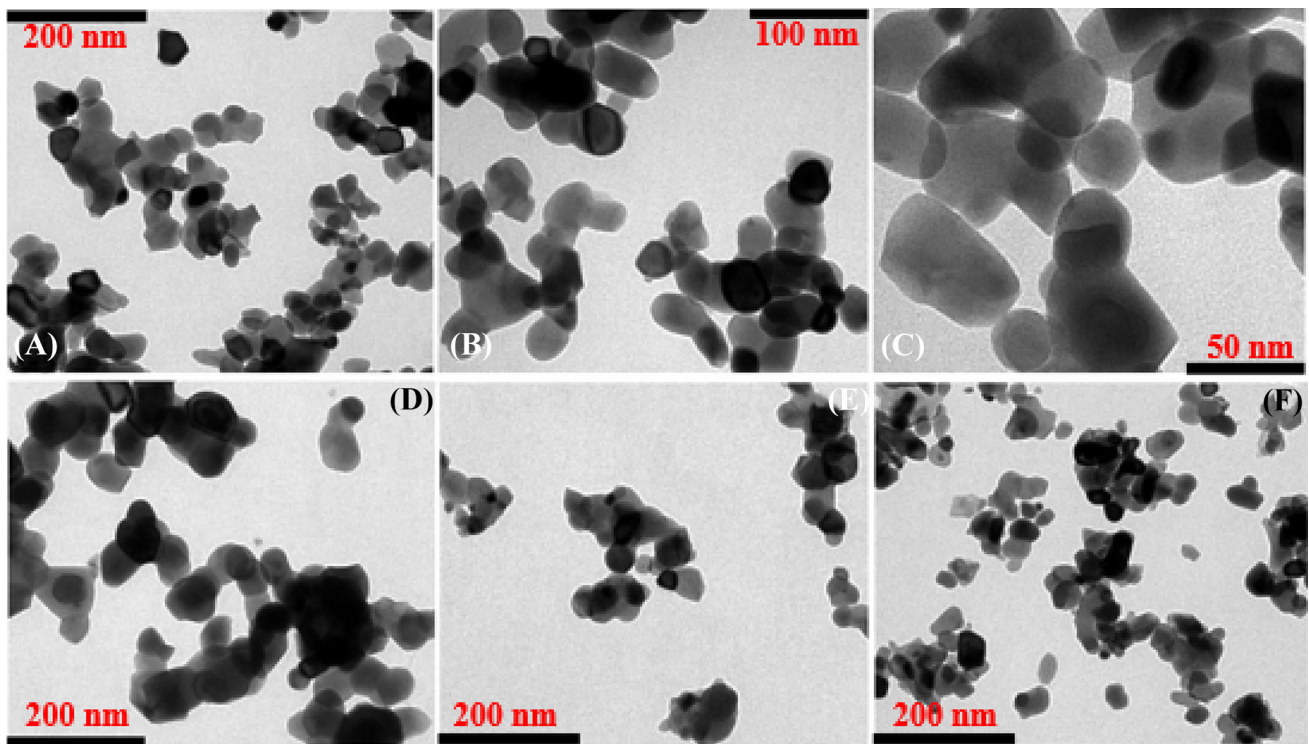
Fig. 2 PXRD patterns of YFeO_3 (A) and $\text{Y}_{1-x}\text{Sr}_x\text{Fe}_{1-y}\text{Ni}_y\text{O}_3$ (B) nanopowders annealed at 800 °C for 1 h

element is also in accordance with their ratio in the nominal compositions (Table 2). Table 2 also shows that the oxygen content in $\text{Y}_{1-x}\text{Sr}_x\text{Fe}_{1-y}\text{Ni}_y\text{O}_3$ materials is much greater than that in the nominal composition, proving the successful substitution of Y^{3+} and Fe^{3+} by Sr^{2+} and Ni^{3+} in the YFeO_3 lattice. When Y^{3+} was replaced by Sr^{2+} and Fe^{3+} was replaced by Ni^{2+} (Ni^{2+} in $\text{Ni}(\text{NO}_3)_2 \cdot 6\text{H}_2\text{O}$), some Fe^{3+} ions would be oxidized to Fe^{4+} and Ni^{2+} to Ni^{3+} to balance the local charge, resulting in the increase of oxygen content in

$\text{Y}_{1-x}\text{Sr}_x\text{Fe}_{1-y}\text{Ni}_y\text{O}_3$ [14, 20, 34, 35]. For Sr and Ni codoped YFeO_3 sample, not all Ni^{2+} ions were oxidized to Ni^{3+} , this sample may have the highest amount of Fe^{3+} oxidized to Fe^{4+} , and thus it has the highest oxygen content (Table 2). Besides, oxygen adsorption on the surface of $\text{Y}_{1-x}\text{Sr}_x\text{Fe}_{1-y}\text{Ni}_y\text{O}_3$ orthoferrite also led to an increased oxygen percentage in the $\text{Y}_{1-x}\text{Sr}_x\text{Fe}_{1-y}\text{Ni}_y\text{O}_3$ structure [34, 36], hence the empirical formula of this material series should be $\text{Y}_{1-x}\text{Sr}_x\text{Fe}_{1-y}\text{Ni}_y\text{O}_{3+\delta}$.

Table 1 Structural characteristics of $Y_{1-x}Sr_xFe_{1-y}Ni_yO_{3\pm\delta}$ nanocrystals

Indices	YFeO ₃	Y _{0.8} Sr _{0.2} FeO ₃	YFe _{0.8} Ni _{0.2} O ₃	Y _{0.8} Sr _{0.2} Fe _{0.8} Ni _{0.2} O ₃
Tolerance factor	0.8182	0.8308	0.8200	0.8312
Crystal system	Orthorhombic	Orthorhombic	Orthorhombic	Orthorhombic
Space group	Pnma (62)	Pnma (62)	Pnma (62)	Pnma (62)
$2\theta_{(121)}$, °	33.1273	33.1140	33.1537	33.1803
D_{XRD} , nm	25.6771	27.6513	25.6589	25.3806
a, Å	5.2808	5.2789	5.2869	5.2823
b, Å	5.5944	5.5961	5.5827	5.5661
c, Å	7.6052	7.6116	7.5964	7.5987
V, Å ³	224.6797	224.8562	224.2091	223.4155
H_c , Oe	50.25	2029.37	2117.32	3957.09
M_r , emu g ⁻¹	0.021	0.145	0.261	2.182
M_s , emu g ⁻¹	0.401	0.492	0.848	4.407

**Fig. 3** TEM images of nanostructured YFeO₃ (a, b, c), Y_{0.8}Sr_{0.2}FeO₃ (d), YFe_{0.8}Ni_{0.2}O₃ (e), and Y_{0.8}Sr_{0.2}Fe_{0.8}Ni_{0.2}O₃ (f) perovskites after annealing at 800 °C for 1 h

The substitution of Sr²⁺ and/or Ni³⁺ in the YFeO_{3+δ} crystal lattice affected not only the structure but also the optical and magnetic properties of the materials (Figs. 5, 6 and Table 3). The UV–Vis absorption spectra of the Sr-doped, Ni-doped, and Sr, Ni co-doped YFeO₃ nanoparticles showed strong absorption in the ultraviolet (~ 250–400 nm) and visible light regions (~ 400–800 nm) (Fig. 5A). While the absorption spectra of pristine and Sr²⁺ and/or Ni³⁺ doped YFeO_{3+δ} show no significant difference

in the UV region, doped YFeO_{3+δ} samples exhibited much higher absorption in the visible range compared to pure YFeO_{3+δ}, with the highest absorption in the case of Ni-doped YFeO_{3+δ} and Sr, Ni co-doped YFeO_{3+δ} samples. This strong transition corresponds to the electronic transition from the 2p valence orbital of oxygen to the 3d conduction band of iron or nickel [12, 28]. There is a bathochromic shift (toward the longer wavelength) in the absorption edge of Sr-doped, Ni-doped, and Sr, Ni co-doped YFeO_{3+δ}

Fig. 4 EDX patterns of $Y_{1-x}Sr_xFe_{1-y}Ni_yO_3$ nanoparticles annealed at 800 °C for 1 h

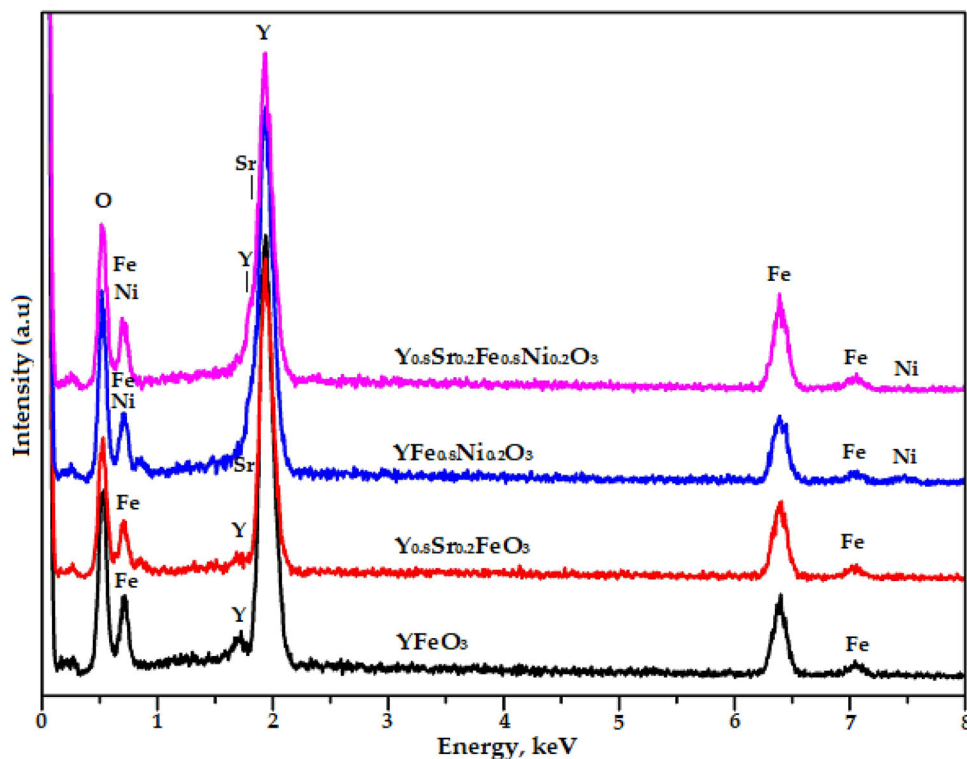


Table 2 EDX results of $Y_{1-x}Sr_xFe_{1-y}Ni_yO_3$ nanopowders annealed at 800 °C for 1 h

Nominal composition of samples	Elemental composition, at.%					Real composition of samples
	Y	Sr	Fe	Ni	O	
YFeO ₃	19.34	–	18.38	–	62.28	YFe _{0.95} O _{3.22}
Y _{0.8} Sr _{0.2} FeO ₃	14.44	3.15	18.52	–	63.89	Y _{0.78} Sr _{0.17} FeO _{3.45}
YFe _{0.8} Ni _{0.2} O ₃	18.83	–	14.88	3.39	62.90	YFe _{0.79} Ni _{0.18} O _{3.34}
Y _{0.8} Sr _{0.2} Fe _{0.8} Ni _{0.2} O ₃	14.39	3.24	14.03	3.42	64.92	Y _{0.80} Sr _{0.18} Fe _{0.78} Ni _{0.19} O _{3.61}

nanoparticles, indicating a decrease in their band gaps. The optical energy gaps (E_{gr} , eV) of the $Y_{1-x}Sr_xFe_{1-y}Ni_yO_{3+\delta}$ nanoparticles were calculated using the Tauc-plot and are shown in Table 3 and Fig. 5B. The optical band gap for the YFeO_{3+δ} sample was calculated to be 1.87 eV, which is lower than previously reported values [12, 28]. For the Sr-doped YFeO_{3+δ} sample, and especially the Ni-doped YFeO_{3+δ} and Sr and Ni co-doped YFeO_{3+δ}, there is a sudden drop in the band gap values (Fig. 5B and Table 3). The band gap of obtained $Y_{1-x}Sr_xFe_{1-y}Ni_yO_{3+\delta}$ nanoparticles (1.87–0.60 eV) is much narrower than those of $Y_{1-x}Sm_xFeO_3$ and $Y_{1-x}Gd_xFe_{0.95}Co_{0.05}O_3$ nanomaterials (see Table 3) [12, 28]. Besides the intrinsic nature of the materials, according to

references [37, 38], reduced particle size leads to a narrow energy gap. Indeed, the size of the obtained YFeO_{3+δ} nanoparticles is remarkably smaller than other YFeO_{3+δ} synthesized by solid-state reaction [28] and sol-gel methods [12]. Furthermore, the size of $Y_{0.8}Sr_{0.2}FeO_{3+\delta} > Y_{0.8}Sr_{0.2}Fe_{0.8}Ni_{0.2}O_{3+\delta} \sim YFe_{0.8}Ni_{0.2}O_{3+\delta}$, hence the band gap values also decrease accordingly (see Tables 1, 3 and Fig. 3). With a narrow band gap, the $Y_{1-x}Sr_xFe_{1-y}Ni_yO_{3+\delta}$ nanoparticles synthesized in this work can be used as a photocatalyst in the visible region for organic decomposition processes.

Figure 6 shows the magnetic properties of the $Y_{1-x}Sr_xFe_{1-y}Ni_yO_{3+\delta}$ nanopowders at room temperature. The doping of Sr and/or Ni into the YFeO₃ crystal

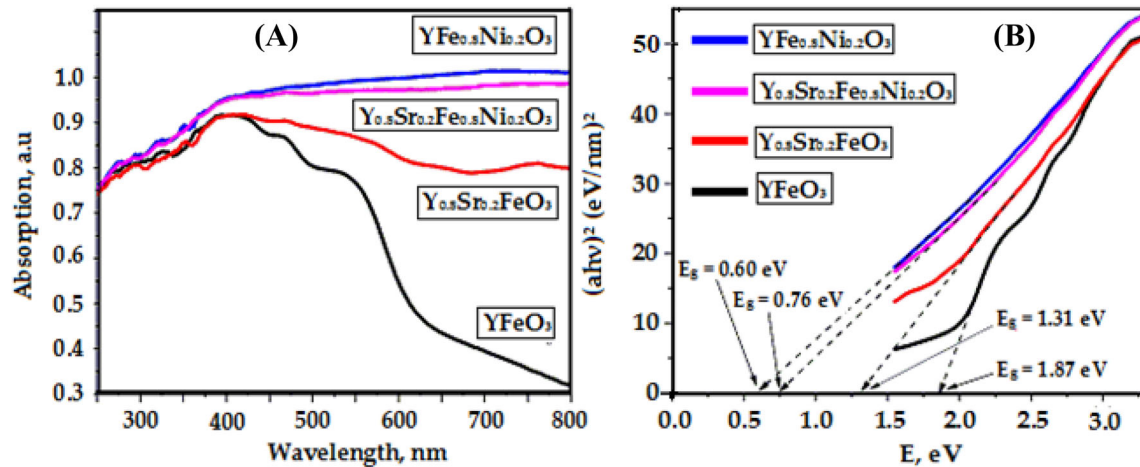
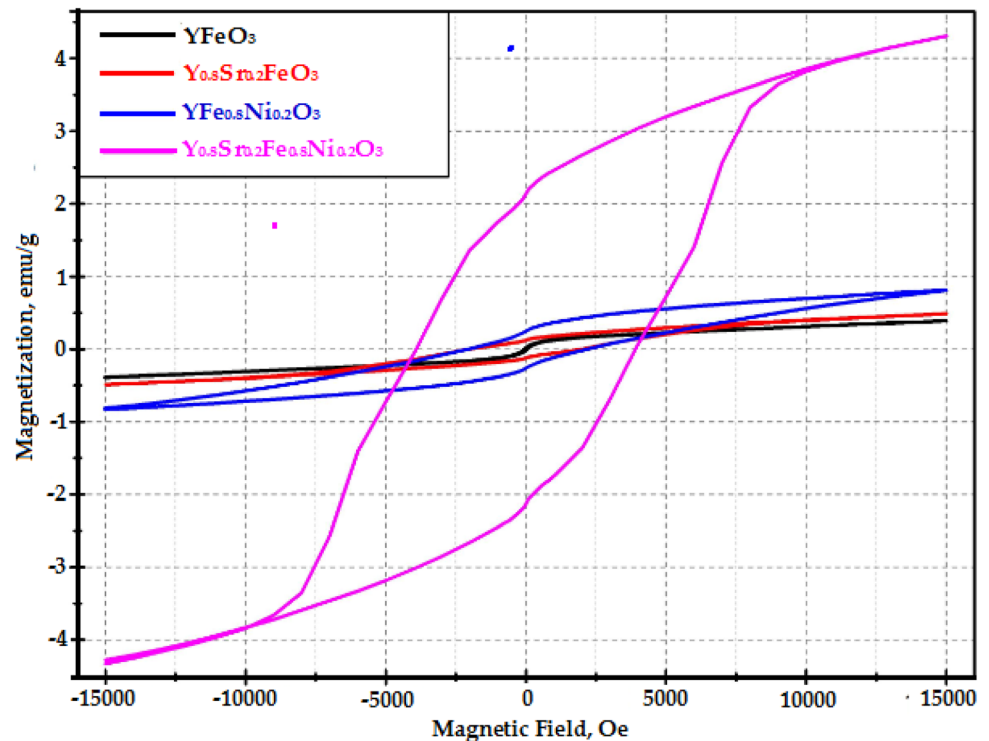


Fig. 5 **A** Room-temperature optical absorbance spectra of the $Y_{1-x}Sr_xFe_{1-y}Ni_yO_{3+\delta}$ samples; **B** Tauc-plot of $(ah\nu)^2$ as a function of photon energy for $Y_{1-x}Sr_xFe_{1-y}Ni_yO_{3+\delta}$ nanoparticles

Fig. 6 Room-temperature magnetic hysteresis loops of as-prepared $Y_{1-x}Sr_xFe_{1-y}Ni_yO_{3+\delta}$ nanoparticles



lattice clearly changed the magnetic nature of the base $YFeO_3$ material. The pure $YFeO_3$ sample, with a narrow hysteresis loop and a very low M_r (0.021 emu g^{-1}) and H_c (50.25 Oe) (Table 3), is a typical weak ferromagnetic material [22]. For Sr and/or Ni-doped $YFeO_3$, a large open region was seen at the center of the hysteresis loops, suggesting ferromagnetic behavior, especially in cases of Sr and Ni co-

doped $YFeO_3$ samples (Fig. 6). The H_c (Oe) and M_r (emu g^{-1}) values of the $Y_{0.8}Sr_{0.2}O_{3+\delta}$ and $YFe_{0.8}Ni_{0.2}O_{3+\delta}$ samples are 40 and 12–21 times greater than those of the pure $YFeO_{3+\delta}$ sample, respectively. For Sr and Ni co-doped $YFeO_3$, the values of H_c and M_r are even much higher (80 times higher for H_c , and 104 times for M_r) (Table 3). The H_c value of $Y_{0.8}Sr_{0.2}Fe_{0.8}Ni_{0.2}O_{3+\delta}$ at 15,000 Oe was approximately

Table 3 Optical band gap and magnetic parameters of $Y_{1-x}Sr_xFe_{1-y}Ni_yO_{3+\delta}$

nanoparticles at 300 K in this work and from the published literature for comparison

Samples	E_g , eV	H_c , Oe	M_r , emu g^{-1}	M_s , emu g^{-1}
$YFeO_{3+\delta}$	1.87	50.25	0.021	0.401
$Y_{0.8}Sr_{0.2}FeO_{3+\delta}$	1.31	2029.37	0.261	0.492
$YFe_{0.8}Ni_{0.2}O_{3+\delta}$	0.60	2117.32	0.459	0.848
$Y_{0.8}Sr_{0.2}Fe_{0.8}Ni_{0.2}O_{3+\delta}$	0.76	3957.09	2.182	4.407
$Y_{1-x}Bi_xFeO_3$ ($x = 0/0.2$) [6]	–	710/–	0.02/–	0.34/0.22
$YFe_{1-x}Mn_xO_3$ ($x = 0/0.2$) [11]	–	–	–	0.015/0.08
$Y_{1-x}Sm_xFeO_3$ ($x = 0/0.15$) [12]	2.11/2.16	3244/37.3	–	0.32/1.05
$YFe_{1-x}Ti_xO_3$ ($x = 0/0.1$) [9]	–	69.56/760	0.19/0.21	2.08/0.81
$YFeO_3$ [28]	2.42	161	0.89	3.50
$Y_{0.8}Gd_{0.2}Fe_{0.95}Co_{0.05}O_3$ [28]	2.24	4200	5.24	1.60

that of $Y_{0.8}Gd_{0.2}Fe_{0.95}Co_{0.05}O_3$ at 60 000 Oe [28] (Table 3). Moreover, the Sr and Ni co-doped $YFeO_3$ sample did not reach saturation at 15,000 Oe, while pure $YFeO_3$, Sr-doped $YFeO_3$, and Ni-doped $YFeO_3$ samples were already saturated at 15,000 Oe. The reasons for the observed improvement in the magnetization can be explained as follows. (1) When the particle size is small, uncompensated surface spins of Fe^{3+} ions are created, leading to a strong magnetic enhancement [39, 40]. In fact, particle and crystallite sizes are in the order of $Y_{0.8}Sr_{0.2}Fe_{0.8}Ni_{0.2}O_{3+\delta} < Y_{0.8}Fe_{0.8}Ni_{0.2}O_{3+\delta} < Y_{0.8}Sr_{0.2}Fe_{0.8}O_{3+\delta}$ (See Table 1 and Fig. 3). (2) The distorted structure is affected by the doping and co-doping effects. The doping of Sr and/or Ni into the $YFeO_3$ structure increased the crystalline magnetic anisotropy, resulting in the large increase in H_c and M_r [39, 40]. (3) Finally, the substitution of Y^{3+} and/or Fe^{3+} by Sr^{2+} and/or Ni^{2+}/Ni^{3+} in $YFeO_3$ enhanced the oxidation process, $Fe^{3+} \rightarrow Fe^{4+} + e$, which led to the increase of super-exchange interactions $Fe^{3+}-O^{2-}-Fe^{4+}$, $Y^{3+}-O^{2-}-Fe^{3+}/Fe^{4+}$, $Sr^{2+}-O^{2-}-Fe^{3+}/Fe^{4+}$, $Ni^{2+}/Ni^{3+}-O^{2-}-Fe^{3+}/Fe^{4+}$, $Ni^{2+}-O^{2-}-Ni^{3+}$, $Y^{3+}-O^{2-}-Ni^{2+}/Ni^{3+}$, $Sr^{2+}-O^{2-}-Ni^{2+}/Ni^{3+}$ compared to the super-exchange interactions $Fe^{3+}-O^{2-}-Fe^{3+}$, $Y^{3+}-O^{2-}-Y^{3+}$ va $Y^{2+}-O^{2-}-Fe^{3+}$ in pure $YFeO_3$ [41].

In this manner, $YFeO_3$ nanopowder, with its weak ferromagnetic behavior, can be used as a material operating under external fields, such as the cores of transformers, electromagnets, or magnetic conductors. Owing to their high H_c and M_r , $Y_{0.8}Sr_{0.2}Fe_{0.8}O_{3+\delta}$, $Y_{0.8}Fe_{0.8}Ni_{0.2}O_{3+\delta}$, and $Y_{0.8}Sr_{0.2}Fe_{0.8}Ni_{0.2}O_{3+\delta}$ can be applied to permanent magnets, magnetic recording materials in hard drives, or magnetic tapes, etc. [22].

4 Conclusions

The single-phase nanostructured $YFeO_{3+\delta}$, $Y_{0.8}Sr_{0.2}Fe_{0.8}O_{3+\delta}$, $Y_{0.8}Fe_{0.8}Ni_{0.2}O_{3+\delta}$, and $Y_{0.8}Sr_{0.2}Fe_{0.8}Ni_{0.2}O_{3+\delta}$ perovskites have been synthesized by the simple co-precipitation method. The hydrolysis of Y^{3+} , Sr^{2+} , Fe^{3+} , and Ni^{2+} cations were carried out in boiling water ($T^\circ \geq 95^\circ C$) with Na_2CO_3 5% as a precipitant. Sr and/or Ni doping distorted the crystal structure of the base material $YFeO_3$, thus correspondingly modified its optical and magnetic properties. The Sr-doped $YFeO_{3+\delta}$, Ni-doped $YFeO_{3+\delta}$, and Sr and Ni co-doped $YFeO_{3+\delta}$ nanopowders have narrow band gaps (of 1.31 eV, 0.60 eV, and 0.76 eV, respectively) and can be used as photocatalysts for the decomposition of organic compounds in the visible light region, which can be recovered easily after their use by rare-earth magnets owing to their high M_r (of 0.261, 0.459, and 2.182 emu g^{-1} , respectively) and H_c (of 2029.37, 2117.32, and 3957.06 Oe, respectively).

Acknowledgements

The authors would like to thank Ho Chi Minh City University of Education for the facility support.

Author contributions

Conceptualization, methodology, and formal analysis: DHTP, LTTN and TAN, validation: TAN and DHC, writing—original draft preparation: TAN, DHC, VXB, writing—review and editing, VOM and IYM. All authors have read and agreed to the published version of the manuscript.

Data availability

The data that support the findings of this study are available from the corresponding author upon reasonable request.

Declarations

Conflict of interest The authors maintain that they have no conflict of interest to be described in this communication.

References

1. V.I. Popkov, O.V. Almyasheva, A.S. Semenova, D.G. Kellerman, Magnetic properties of YFeO_3 nanocrystals obtained by different soft-chemical methods. *J. Mater. Sci.* **28**, 7163–7170 (2017)
2. M. Wang, T. Wang, Sh. Song, M. Tan, Structure-controllable synthesis of multiferroic YFeO_3 nanopowders and their optical and magnetic properties. *Materials* **10**(6), 626 (2017)
3. R. Maiti, S. Basu, D. Chakravorty, Synthesis of nanocrystalline YFeO_3 and its magnetic properties. *J. Magn. Magn. Mater.* **321**, 3274–3277 (2009)
4. X. Lu, J. Xie, H. Shu, J. Liu, Ch. Yin, J. Lin, Microwave-assisted synthesis of nanocrystalline YFeO_3 and study of its photoactivity. *Mater. Sci. Eng. B.* **138**, 289–292 (2007)
5. M.I. Diez-Garcia, V. Celorrio, L. Calvillo, D. Tiwari, R. Gomez, D. Fermin, YFeO_3 photocathodes for hydrogen evolution. *Electrochim. Acta* **246**, 365–371 (2017)
6. O. Rosales-Gonzalez, F.S.D. Jesus, F. Pedro-Garcia, C.A. Cortes-Escobedo, M. Ramirez-Cardona, A.M. Bolarin-Miro, Enhanced multiferroic properties of YFeO_3 by doping with Bi^{3+} . *Materials* **12**, 2054 (2019)
7. A.T. Nguyen, V.N.T. Pham, TTr.L. Nguyen, V.O. Mittova, Q.M. Vo, M.V. Berezhnaya, IYa. Mittova, T.H. Do, H.D. Chau, Crystal structure and magnetic properties of perovskite $\text{YFe}_{1-x}\text{Mn}_x\text{O}_3$ nanopowders synthesized by co-precipitation method. *Solid State Sci.* **96**, 105922 (2019)
8. A.T. Nguyen, H.D. Chau, Tr.L.T. Nguyen, V.O. Mittova, T.H. Do, IYa. Mittova, Structural and magnetic properties of $\text{YFe}_{1-x}\text{Co}_x\text{O}_3$ ($0.1 \leq x \leq 0.5$) perovskite nanomaterials synthesized by co-precipitation method. *Nanosyst. Phys. Chem. Math.* **9**(3), 424–429 (2018)
9. N.O. Khalifa, H.M. Widatallah, A.M. Gismelseed, F.N. Al-Mabsali, R.G.S. Sofin, M. Pekala, Magnetic and Mössbauer studies of pure and Ti-doped YFeO_3 nanocrystalline particles prepared by mechanical milling and subsequent sintering. *Hyperfine Inter.* **237**, 46 (2016)
10. M.V. Berezhnaya, O.V. Al'myasheva, V.O. Mittova, A.T. Nguyen, IYa. Mittova, Sol-gel synthesis and properties of $\text{Y}_{1-x}\text{Ba}_x\text{FeO}_3$ nanocrystals. *Rus. J. Gen. Chem.* **88**(4), 626–631 (2018)
11. H. Shen, J. Xu, M. Jin, G. Jiang, Influence of manganese on the structure and magnetic properties of YFeO_3 nanocrystal. *Ceram. Inter.* **38**, 1473–1477 (2012)
12. P.S.J. Bharadwaj, S. Kundu, V.S. Kollipara, Structural, optical and magnetic properties of Sm^{3+} doped yttrium orthoferrite (YFeO_3) obtained by sol-gel synthesis route. *J. Phys. Condens. Matt.* **32**, 035810 (2020)
13. C. Sasikala, N. Durairaj, I. Baskaran, B. Sathyaseelan, M. Henini, Transition metal titanium (Ti) doped LaFeO_3 nanoparticles for enhanced optical structure and magnetic properties. *J. All. Compd.* **712**, 870–877 (2017)
14. T.A. Nguyen, V.N.T. Pham, H.T. Le, D.H. Chau, V.O. Mittova, L.TTr. Nguyen, D.A. Dinh, T.V.N. Hao, IYa. Mittova, Crystal structure and magnetic properties of $\text{LaFe}_{1-x}\text{Ni}_x\text{O}_3$ nanomaterials prepared via a simple co-precipitation method. *Ceram. Inter.* **45**, 21768–21772 (2019)
15. C. Feng, S. Ruan, J. Li, B. Zou, J. Luo, W. Chen, W. Dong, F. Wu, Ethanol sensing properties of $\text{LaCo}_x\text{Fe}_{1-x}\text{O}_3$ nanoparticles: effects of calcination temperature, Co-doping, and carbon nanotube-treatment. *Sens. Act. B* **155**(1), 232–238 (2011)
16. N.A. Tien, I.Y. Mittova, D.O. Solodukhin, O.V. Al'myasheva, O.V. Mittova, SYu. Demidova, Sol-gel formation and properties of nanocrystals of solid solution $\text{Y}_{1-x}\text{Ca}_x\text{FeO}_3$. *Rus. J. Inor. Chem.* **59**(2), 40–45 (2014)
17. A. Somvanshi, Sh. Husain, W. Khan, Investigation of structure and physical properties of cobalt doped nano-crystalline neodymium orthoferrite. *J. Alloys Compd.* **778**, 439 (2019)
18. M.V. Knurova, I.Y. Mittova, N.S. Perov, O.V. Al'myasheva, N.A. Tien, V.O. Mittova, V.V. Bessalova, E.L. Viryutina, Effect of the degree of doping on the size and magnetic properties of nanocrystals $\text{La}_{1-x}\text{Zn}_x\text{FeO}_3$ synthesized by the sol-gel method. *Rus. J. Inor. Chem.* **62**(3), 281–287 (2017)
19. W. Haron, Th. Thaweechai, W. Wattanathana, A. Laobuthee, H. Manaspiya, Ch. Veranitisagul, N. Koonsaeng, Structure characteristics and dielectric properties of $\text{La}_{1-x}\text{Co}_x\text{FeO}_3$ and $\text{LaFe}_{1-x}\text{Co}_x\text{O}_3$ synthesized via metal organic complexes. *Energy Proc.* **34**, 791–800 (2013)
20. Z. Habib, K. Majid, M. Ikram, Kh. Sultan, Influence of Ni substitution at B-site for Fe^{3+} ions on morphological, optical, and magnetic properties of HoFeO_3 ceramics. *Appl. Phys. A* **122**, 550 (2016)
21. A. Bashir, M. Ikram, R. Kumar, P.N. Lisboa-Filho, Structural, electronic structure and magnetic studies of $\text{GdFe}_{1-x}\text{Ni}_x\text{O}_3$ ($x \leq 0.5$). *J. Alloys Compd.* **521**, 183–188 (2012)
22. B.D. Cullity, C.D. Graham, *Introduction to magnetic materials*, 2nd edn. (Wiley, Canada, 2009)

23. N.A. Tien, V. Pham, D.H. Chau, V.O. Mittova, I.Y. Mittova, E.I. Kopeychenko, L.TTr. Nguyen, V.X. Bui, A.T.P. Nguyen, Effect of Ni substitution on phase transition crystal structure and magnetic properties of nanostructured YFeO₃ perovskite. *J. Mol. Struct.* **1215**, 128293 (2020)
24. M. Johnsson, P. Lemmens, *Crystallography and chemistry of perovskites*, 1st edn. (Wiley, Hoboken, 2007)
25. C.E. Housecroft, A.G. Sharpe, *Inorganic Chemistry*, 2nd edn. (Prentice Hall, Pearson, 2005)
26. N. Imanaka, *Physical and chemical properties of rare earth oxides, binary rare earth oxides* (Kluwer Academic Publishers, Dordrecht, 2004), pp. 111–113
27. T.A. Nguyen, L.TTr. Nguyen, V.X. Bui, Influence of the synthetic conditions on the crystal structure, magnetic and optical properties of holmium orthoferrite nanoparticles. *J. Mater. Sci.* **32**, 19010–19019 (2021)
28. M. Wang, T. Wang, Structural, magnetic and optical properties of Gd and Co co-doped YFeO₃ nanopowders. *Materials* **12**, 2423 (2019)
29. N. Ghobadi, Band gap determination using absorption spectrum fitting procedure. *Inter. Nano Lett.* (2013). <https://doi.org/10.1186/2228-5326-3-2>
30. A.G. Belous, E.V. Pashkova, V.A. Elshanskii, V.P. Ivanitskii, Effect of precipitation conditions on the phase composition, particle morphology, and properties of iron (III, II) hydroxide precipitates. *Inor. Mater.* **36**, 343–351 (2000)
31. P. Caro, M. Lemaitre, M. Blassé, C.R. Reances, Hydroxycarbonates terres rares Ln₂(CO₃)_x(OH)_{2(3-x)}.nH₂O. *Acad. Sci. Ser. C* **269**, 687–690 (1969)
32. T.A. Nguyen, V. Pham, T.L. Pham, L.TTr. Nguyen, I.Y. Mittova, V.O. Mittova, L.N. Vo, B.T.T. Nguyen, V.X. Bui, E.L. Viryutina, Simple synthesis of NdFeO₃ by the so-precipitation method based on a study of thermal behaviors of Fe (III) and Nd (III) hydroxides. *Curr. Comput.-Aided Drug Des.* **10**, 219 (2020)
33. W. Shijin, Zh. Shengliang, W. Zubiao, W. Yuling, W. Shangping, Ch. Jianjun, X. Rong, L. Longfei, Synthesis and characterization of yttrium hydroxide and oxide microtubes. *Rare Met.* **28**(5), 445–448 (2009)
34. V.V. Kharton, A.V. Kovalevsky, M.V. Patrakeev, E.V. Tsipis, A.P. Viskup, V.A. Kolotygin, A.A. Yaremchenko, A.L. Shaula, E.A. Kiselev, J.C. Waerenborg, Oxygen nonstoichiometry, mixed conductivity, and Mössbauer spectra of Ln_{0.5}A_{0.5}FeO_{3-δ} (Ln = La – Sm, A = Sr, Ba): effect of cation size. *Chem. Mater.* **20**, 6457–6467 (2008)
35. H.W. Brinks, H. Fjellvag, A. Kjekshus, B.C. Hauback, Structure and magnetism of Pr_{1-x}Sr_xFeO_{3-δ}. *J. Solid State Chem.* **150**(2), 233–249 (2000)
36. J.W. Fergus, Perovskite oxides for semiconductor-based gas sensors. *Sensors Actuators B* **123**, 1169–1179 (2007)
37. C.V. Ramana, R.J. Smith, O.M. Hussain, Grain size effects on the optical characteristics of pulsed-laser deposited vanadium oxide thin films. *Phys. Status Solidi A* (2003). <https://doi.org/10.1002/pssa.200309009>
38. A.J. Deotale, R.V. Nandedkar, Correlation between particle size, strain and band gap of iron oxide nanoparticles. *Mater. Today* **3**(6), 2069–2076 (2016)
39. T. Moriya, New mechanism of anisotropic superexchange interaction. *Phys. Rev. Lett.* **4**, 228–230 (1960)
40. I. Dzyaloshinsky, A thermodynamic theory of weak ferromagnetism of antiferromagnetics. *J. Phys. Chem. Solids* **4**(4), 241–255 (1958)
41. A. Jaiswal, R. Das, S. Adyanthaya, P. Poddar, Surface effects on morin transition, exchange bias, and enhanced spin reorientation in chemically synthesized DyFeO₃ nanoparticles. *J. Phys. Chem. C* **115**(7), 2954–2960 (2011)

Publisher's Note Springer Nature remains neutral with regard to jurisdictional claims in published maps and institutional affiliations.